
DISENTANGLED REPRESENTATION LEARNING AND GENERATION WITH MANIFOLD OPTIMIZATION

Arun Pandey

Department of Electrical Engineering
ESAT-STADIUS, KU Leuven

Kasteelpark Arenberg 10, B-3001 Leuven, Belgium
arun.pandey@esat.kuleuven.be

Michaël Fanuel

Department of Electrical Engineering
ESAT-STADIUS, KU Leuven

Kasteelpark Arenberg 10, B-3001 Leuven, Belgium
michael.fanuel@esat.kuleuven.be

Joachim Schreurs

Department of Electrical Engineering
ESAT-STADIUS, KU Leuven

Kasteelpark Arenberg 10, B-3001 Leuven, Belgium
joachim.schreurs@esat.kuleuven.be

Johan A. K. Suykens

Department of Electrical Engineering
ESAT-STADIUS, KU Leuven

Kasteelpark Arenberg 10, B-3001 Leuven, Belgium
johan.suykens@esat.kuleuven.be

February 5, 2021

Abstract

Disentanglement is a useful property in representation learning which increases the interpretability of generative models such as Variational Auto-Encoders (VAE), Generative Adversarial Models, and their many variants. Typically in such models, an increase in disentanglement performance is traded-off with generation quality. In the context of latent space models, this work presents a representation learning framework that explicitly promotes disentanglement by encouraging orthogonal directions of variations. The proposed objective is the sum of an auto-encoder error term along with a Principal Component Analysis reconstruction error in the feature space. This has an interpretation of a Restricted Kernel Machine with an interconnection matrix on the Stiefel manifold. Our analysis shows that such a construction promotes disentanglement by matching the principal directions in latent space with the directions of orthogonal variation in data space. The training algorithm involves a stochastic optimization method on the Stiefel manifold, which increases only marginally the computing time compared to an analogous VAE. Our theoretical discussion and various experiments show that the proposed model improves over many VAE variants in terms of both generation quality and disentangled representation learning.

Keywords Generative models · Latent variable models · Disentanglement.

1 Introduction

Latent space models are popular tools for sampling from high dimensional distributions. Often, only a small number of latent factors are sufficient to describe data variations. These models exploit the underlying structure of the data and learn explicit representations that are faithful to the data generating factors. Popular latent space models are Variational Auto-Encoders (VAEs) [13], Restricted Boltzmann Machines (RBMs) [27], Normalizing Flows [25], and their many variants.

Disentanglement. In latent variable modelling, one is often interested in modelling the data in terms of *uncorrelated* or *independent* components, yielding a so-called ‘disentangled’ representation [3] which is often studied in the context of VAEs. In representation learning, disentanglement corresponds to a decoupling of generating factors. Components corresponding to orthogonal directions in latent space may be interpreted as

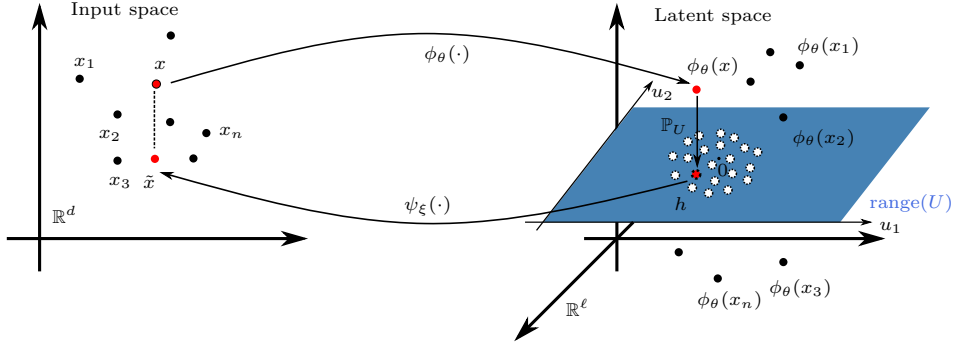


Figure 1: Schematic illustration of St-RKM training problem. The length of the dashed line represents the reconstruction error (see Auto-Encoder term in (St-RKM)) and the length of the vector projecting on hyperplane represents the PCA reconstruction error. After training, the projected points tend to be distributed normally on the hyperplane.

generating distinct factors in input space e.g. lighting conditions, style, colors, etc. An illustration of a latent traversal is shown in Figure 2, where one observes that only one specific feature of the image is changing as one moves along a component in latent space. For instance, in the first row of right-hand side of Figure 2, we observe that moving along the first principal component generates images where only floor color is varying while all other features such as shape, scale, wall color, object color, etc. are constant. In the second row, the object scale is only changing. An advantage of such a representation is that the different latent units impart more interpretability to the model. Disentangled models are useful for the generation of plausible pseudo-data with certain desirable properties, e.g. generating new car designs with a predefined color or height. One popular variant achieving disentanglement but at the expense of generation quality is β -VAE [10].

Motivation. Let $p(\mathbf{x})$ be the distribution of the data $\mathbf{x} \in \mathbb{R}^d$ and consider latent vectors $\mathbf{z} \in \mathbb{R}^\ell$ with the prior distribution $p(\mathbf{z})$, chosen to be a standard normal. Then, one defines an encoder $q(\mathbf{z}|\mathbf{x})$ that can be deterministic or random, for e.g. given by $\mathcal{N}(\mathbf{z}|\phi_\theta(\mathbf{x}), \gamma^2 \mathbb{I})$, where the mean¹ is given by the neural network ϕ_θ parametrized by reals θ . A random decoder $p(\mathbf{x}|\mathbf{z}) = \mathcal{N}(\mathbf{x}|\psi_\xi(\mathbf{z}), \sigma_0^2 \mathbb{I})$ is associated to the decoder neural network ψ_ξ , parametrized by reals ξ , which maps latent codes to the data points. A VAE is estimated by maximizing the lower bound

$$\mathbb{E}_{\mathbf{z} \sim q(\mathbf{z}|\mathbf{x})} [\log(p(\mathbf{x}|\mathbf{z}))] - \beta \text{KL}(q(\mathbf{z}|\mathbf{x}), p(\mathbf{z})) \leq \log p(\mathbf{x}), \quad (1)$$

which is called the Evidence Lower Bound (ELBO) when $\beta = 1$. It has been argued in [10] that larger values of $\beta > 1$ promote more disentanglement. In this paper, we attempt to reconcile generation quality with disentanglement. To introduce the model, we firstly make explicit the connection between β -VAEs and standard Auto-Encoders (AEs). Let the dataset be $\{\mathbf{x}_i\}_{i=1}^n$ with $\mathbf{x}_i \in \mathbb{R}^d$. Let $q(\mathbf{z}|\mathbf{x}) = \mathcal{N}(\mathbf{z}|\phi_\theta(\mathbf{x}), \gamma^2 \mathbb{I})$ be an encoder, where $\mathbf{z} \in \mathbb{R}^\ell$. For a fixed $\gamma > 0$, the maximization problem (1) is then equivalent to the minimization of the ‘regularized’ AE

$$\min_{\theta, \xi} \frac{1}{n} \sum_{i=1}^n \left\{ \mathbb{E}_\epsilon \|\mathbf{x}_i - \psi_\xi(\phi_\theta(\mathbf{x}_i) + \epsilon)\|_2^2 + \alpha \|\phi_\theta(\mathbf{x}_i)\|_2^2 \right\}, \quad (2)$$

where $\alpha = \beta \sigma_0^2$, $\epsilon \sim \mathcal{N}(0, \gamma^2 \mathbb{I})$ and where additive constants depending on γ have been omitted. The first term in (2) might be interpreted as an AE loss whereas the second term can be viewed as a regularization. This ‘regularized’ AE interpretation motivates our method as introduced below.

2 Proposed model

The optimization problem proposed here is best understood by considering the analogy between Variational Auto-Encoders and classical Auto-Encoders.

¹The common definition of a VAE includes another neural network for parametrizing the covariance matrix. To simplify this introductory discussion, this matrix is here chosen as a constant diagonal $\gamma^2 \mathbb{I}$.

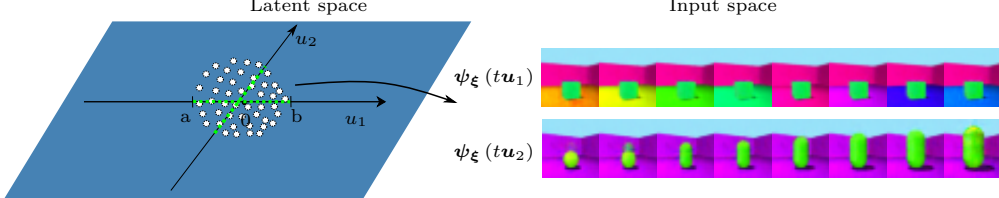


Figure 2: Image by the decoder of the latent space traversal, i.e., $\psi_\xi(tu_i)$ for $t \in [a, b]$ with $a < b$ and for some $i \in \{1, \dots, m\}$. Green and black dashed-lines represent the walk along u_1 and u_2 respectively. At every step of the walk, the image of the decoder is computed to generate the data in the input space. The images were generated by St-RKM with $\sigma = 10^{-3}$.

2.1 Training jointly an auto-encoder and Principal Component Analysis in latent space

The idea consists of learning an auto-encoder along with finding an ‘optimal’ linear subspace of the latent space so that the variance of the training set in latent space is maximized within this space. See Figure 1 to follow the discussion below. The encoder $\phi_\theta : \mathbb{R}^d \rightarrow \mathbb{R}^\ell$ typically sends input data to a latent space while the decoder $\psi_\xi : \mathbb{R}^\ell \rightarrow \mathbb{R}^d$ goes in the reverse direction, and constitutes an approximate inverse. Both the encoder and decoder are neural networks parametrized by vectors of reals θ and ξ . However, it is unclear how to define a parametrization or an architecture of these neural networks so that the learned representation is disentangled. Therefore, in addition to these trained parameters, we also jointly find an m -dimensional linear subspace $\text{range}(U)$ of the latent space \mathbb{R}^ℓ , so that the encoded training points mostly lie within this subspace. This linear subspace is given by the span of the orthonormal columns of the $\ell \times m$ matrix

$$U = \begin{bmatrix} | & & | \\ u_1 & \dots & u_m \\ | & & | \end{bmatrix}.$$

The set of $\ell \times m$ matrices with orthonormal columns with $\ell \geq m$ defines the Stiefel manifold $\text{St}(\ell, m)$. For a reference about Stiefel manifold, we refer to [1]. The idea is then to encode input data into a subspace of the latent space by

$$\mathbf{x} \mapsto \mathbb{P}_U \phi_\theta(\mathbf{x}) = u_1^\top \phi_\theta(\mathbf{x}) \times \begin{bmatrix} | \\ u_1 \\ | \end{bmatrix} + \dots + u_m^\top \phi_\theta(\mathbf{x}) \times \begin{bmatrix} | \\ u_m \\ | \end{bmatrix},$$

where the projector onto $\text{range}(U)$ is simply $\mathbb{P}_U = UU^\top$.

The orthonormal vectors $\{u_1, \dots, u_m\}$ provides directions associated with different generative factors of our generative model, or in other words the principal directions in latent space match orthogonal directions of variation in the data space (see Figure 1), in the spirit of Principal Component Analysis (PCA). This argument is more motivated in Section 3.2. We propose to train an objective function which is a *trade-off* between

- an AE loss which promotes parameters such that $\psi_\xi(\mathbb{P}_U \phi_\theta(\mathbf{x}_i)) \approx \mathbf{x}_i$,
- and, a PCA loss which aims to yield $\mathbb{P}_{U^\perp} \phi_\theta(\mathbf{x}_i) \approx 0$,

for all $i \in [n]$. The parameters trained are the real entries of θ, ξ as well as the matrix $U \in \text{St}(\ell, m)$. The model proposed in this paper is

$$\min_{\theta, \xi} \lambda \underbrace{\frac{1}{n} \sum_{i=1}^n L_{\xi, U}(\mathbf{x}_i, \phi_\theta(\mathbf{x}_i))}_{\text{Auto-Encoder objective}} + \underbrace{\frac{1}{n} \sum_{i=1}^n \|\mathbb{P}_{U^\perp} \phi_\theta(\mathbf{x}_i)\|_2^2}_{\text{PCA objective}}, \quad (\text{St-RKM})$$

where $\lambda > 0$ is a trade-off parameter. It is named Stiefel-Restricted Kernel Machines (St-RKM) in view of Section 2.3, where more details about Restricted Kernel Machines are given. Though, detailed knowledge of RKM is not needed to understand the content of this paper. Hereabove, the AE encoder objective can be chosen as

$$L_{\xi, U}^{(\sigma)}(\mathbf{x}, \mathbf{z}) = \mathbb{E}_{\epsilon \sim \mathcal{N}(0, \mathbb{I})} \|\mathbf{x} - \psi_\xi(\mathbb{P}_U \mathbf{z} + \sigma U \epsilon)\|_2^2, \text{ with } \sigma > 0,$$

in analogy with the VAE objective (2). In Section 2.2, other AE losses are discussed. The basic idea is to combine in (St-RKM) different AE losses with a regularization term which penalizes the feature map in the orthogonal subspace U^\perp . The PCA interpretation becomes clear if we introduce the covariance matrix

$$C_\theta = \frac{1}{n} \sum_{i=1}^n \phi_\theta(\mathbf{x}_i) \phi_\theta^\top(\mathbf{x}_i),$$

where the feature map is assumed to be centered, i.e. $\mathbb{E}_{\mathbf{x} \sim p(\mathbf{x})}[\phi_\theta(\mathbf{x})] = \mathbf{0}$. Then, for a given positive integer $m \leq \ell$ the classical PCA problem reads

$$\min_{U \in \text{St}(\ell, m)} \text{Tr}(C_\theta - \mathbb{P}_U C_\theta \mathbb{P}_U),$$

as it is explained, for instance, in Section 4.1 of [2]. Clearly, if \mathbb{P}_U is the projector on the m principal components, then the columns of U are the eigenvectors of the covariance matrix² and we have the following diagonalization

$$U^\top C_\theta U = \text{diag}(\boldsymbol{\lambda}),$$

where $\boldsymbol{\lambda}$ is a vector containing the principal values. The PCA objective function can be written as a sum of squared errors as follows

$$\text{Tr}(C_\theta - \mathbb{P}_U C_\theta \mathbb{P}_U) = \frac{1}{n} \sum_{i=1}^n \|\mathbb{P}_{U^\perp} \phi_\theta(\mathbf{x}_i)\|_2^2,$$

where $\mathbb{P}_{U^\perp} = \mathbb{I} - \mathbb{P}_U$. The above PCA objective corresponds to the reconstruction error of Kernel PCA, for the kernel $k_\theta(\mathbf{x}, \mathbf{y}) = \phi_\theta^\top(\mathbf{x}) \phi_\theta(\mathbf{y})$.

2.2 Proposition of two AE losses

Here, we consider two stochastic AE losses. The first loss reads

$$L_{\xi, U}^{(\sigma)}(\mathbf{x}, \mathbf{z}) = \mathbb{E}_\epsilon \|\mathbf{x} - \psi_\xi(\mathbb{P}_U \mathbf{z} + \sigma U \epsilon)\|_2^2,$$

where $\epsilon \sim \mathcal{N}(0, \mathbb{I}_m)$. As motivated by Lemma 1 below, the noise term $\sigma U \epsilon$ above promotes a *smoother* decoder network. To further improve disentanglement, we propose a splitted AE loss

$$L_{\xi, U}^{(\sigma), sl}(\mathbf{x}, \mathbf{z}) = L_{\xi, U}^{(0)}(\mathbf{x}, \mathbf{z}) + \mathbb{E}_\epsilon \|\psi_\xi(\mathbb{P}_U \mathbf{z}) - \psi_\xi(\mathbb{P}_U \mathbf{z} + \sigma U \epsilon)\|_2^2, \quad (3)$$

with $\epsilon \sim \mathcal{N}(0, \mathbb{I}_m)$. The first term in (3) is the classical AE loss ($\sigma = 0$) while the second term promotes orthogonal directions of variations, as is discussed further in Section 3.1.

In the proposed model, reconstruction of an out-of-sample point \mathbf{x} is given by $\psi_\xi(\mathbb{P}_U \phi_\theta(\mathbf{x}))$. Note that we don't simply propose another encoder-decoder architecture, given by: $U^\top \phi_\theta(\cdot)$ and $\psi_\xi(U \cdot)$. Instead, our objective assumes that the neural network defining the encoder provides a better embedding if we impose that it maps training points on a linear subspace of dimension $m < \ell$ in the ℓ -dimensional latent space. In other words, the optimization of the parameters in the last layer of the encoder does not play a redundant role, since the second term in (St-RKM) clearly also depends on $\mathbb{P}_{U^\perp} \phi_\theta(\cdot)$.

The problem (St-RKM) was inspired by Restricted Kernel Machines (RKM) by [28], which are briefly described in the next section.

2.3 Restricted Kernel Machines

RKMs yield a representation of kernel methods with visible and hidden units; thereby establishing links between Kernel Principal Component Analysis (KPCA) and RBMs. This framework has an energy form similar to RBMs [15] and there is a training procedure in a non-probabilistic setting. The optimization problem (St-RKM) can be expressed as the sum of a regularized AE loss and RKM as follows

$$\min_{\theta, \xi} \min_{U \in \text{St}(\ell, m)} \sum_{i=1}^n \left\{ \frac{\lambda}{2} L_{\xi, U}(\mathbf{x}_i, \phi_\theta(\mathbf{x}_i)) + \underbrace{f(\mathbf{h}_i) - \phi_\theta^\top(\mathbf{x}_i) U \mathbf{h}_i}_{\text{RKM}} + \frac{1}{2} \|\phi_\theta(\mathbf{x}_i)\|_2^2 \right\},$$

²This follows from Proposition 1 given hereafter and the fact $\text{Tr}(\mathbb{P}_U C_\theta \mathbb{P}_U) = \text{Tr}(U^\top C_\theta U)$. The latter identity uses the cyclicity of the trace and $U^\top U = \mathbb{I}_m$.

Table 1: FID Scores [9] for 8000 randomly generated samples (smaller is better). St-RKM variants are shaded and outperform competitors in all datasets but one.

Models	MNIST	fMNIST	SVHN	Dsprites	3Dshapes	Cars3D
St-RKM ($\sigma = 0$)	28.71 (± 0.33)	67.70 (± 0.50)	62.97 (± 0.34)	88.82 (± 1.32)	25.76 (± 1.74)	174.42 (± 0.32)
St-RKM ($\sigma = 10^{-3}$)	28.83 (± 0.23)	66.84 (± 0.28)	60.42 (± 0.32)	84.91 (± 1.81)	21.87 (± 0.18)	169.86 (± 0.44)
St-RKM-sl ($\sigma = 10^{-3}$)	28.58 (± 0.21)	73.85 (± 0.36)	60.40 (± 0.34)	75.94 (± 0.82)	23.14 (± 0.38)	174.76 (± 0.52)
VAE ($\beta = 1$)	39.38 (± 0.31)	101.26 (± 0.54)	71.13 (± 0.36)	119.55 (± 1.46)	37.62 (± 1.63)	213.09 (± 0.30)
β -VAE ($\beta = 3$)	30.14 (± 0.19)	86.12 (± 0.62)	72.93 (± 0.47)	83.25 (± 1.87)	30.39 (± 1.01)	172.39 (± 0.41)
FactorVAE	35.12 (± 1.32)	91.43 (± 2.16)	87.45 (± 1.4)	61.83 (± 1.23)	41.45 (± 1.66)	175.21 (± 0.22)
Info-GAN	77.75 (± 2.05)	78.77 (± 12.51)	98.10 (± 1.21)	121.46 (± 2.84)	55.11 (± 3.18)	177.14 (± 0.21)

where $\phi_{\theta}(\mathbf{x}_i) \in \mathbb{R}^{\ell}$, $\mathbf{h}_i \in \mathbb{R}^m$ with $m \leq \ell$ and U is an interconnection matrix³. The function $f : \mathbb{R}^m \rightarrow]-\infty, +\infty]$ is used for regularization and for instance can be chosen as closed and strongly convex, or as the characteristic function of a closed set. The analogy with RBM goes as follows: $\phi_{\theta}(\mathbf{x}_i)$ is interpreted as visible ‘units’ whereas U plays the role of an interconnection matrix with hidden features \mathbf{h}_i , which are not binary-valued contrary to RBMs. The first minimization in the above problem gives $\mathbf{h}_i^* = U^{\top} \phi_{\theta}(\mathbf{x}_i)$, which yields the first term of the optimal objective $-f^*(U^{\top} \phi_{\theta}(\mathbf{x}_i))$ in terms of f^* , i.e., the Fenchel conjugate of f . In this paper, we focus mainly on the squared norm regularizer $f(\mathbf{h}) = \frac{1}{2} \|\mathbf{h}\|_2^2$, which yields our main objective (St-RKM).

3 PCA and disentanglement

3.1 Decoder smoothness and disentanglement

In the case of the stochastic loss, the smoothness of the decoder is motivated by the following Lemma which extends the result of [26]. Here we adapt it in the context of optimization on the Stiefel manifold.

Lemma 1 *Let $\epsilon \sim \mathcal{N}(\mathbf{0}, \mathbb{I}_m)$ a random vector and $U \in \text{St}(\ell, m)$. Let $\psi_a(\cdot) \in \mathcal{C}^2(\mathbb{R}^{\ell})$ with $a \in [d]$. If the function $[\psi(\cdot) - \mathbf{x}]_a^2$ has L -Lipschitz continuous Hessian for all $a \in [d]$, we have*

$$\begin{aligned} \mathbb{E}_{\epsilon}[\mathbf{x} - \psi(\mathbf{y} + \sigma U \epsilon)]_a^2 &= [\mathbf{x} - \psi(\mathbf{y})]_a^2 + \sigma^2 \text{Tr}(U^{\top} \nabla \psi_a(\mathbf{y}) \nabla \psi_a(\mathbf{y})^{\top} U) \\ &\quad - \sigma^2 [\mathbf{x} - \psi(\mathbf{y})]_a \text{Tr}(U^{\top} \text{Hess}_{\mathbf{y}}[\psi_a] U) + R_a(\sigma), \end{aligned} \quad (4)$$

with $|R_a(\sigma)| \leq \frac{1}{6} \sigma^3 L \frac{\sqrt{2}(m+1)\Gamma((m+1)/2)}{\Gamma(m/2)}$ where Γ is Euler’s Gamma function.

In Lemma 1, the additional terms proportional to σ^2 can be interpreted as biases. Specifically, the second term on the right-hand side of the equation in Lemma 1 indicates that the stochastic AE loss promotes a smooth decoder by penalizing its derivative.

Remark 1 *For a classical neural network architecture, it is unclear in practice if the function $[\psi(\cdot) - \mathbf{x}]_a^2$ has L -Lipschitz continuous Hessian for all $a \in [d]$. This assumption in Lemma 1 is used to provide a meaningful bound on the reminder in (4).*

3.2 Disentanglement

Here we argue that *the principal directions in latent space match orthogonal directions of variation in the data space*. Therefore, the disentanglement of our representation is due to the optimization over $U \in \text{St}(\ell, m)$ and is promoted by the stochastic AE loss. Let $\Delta_k = \nabla \psi(\mathbf{y})^{\top} \mathbf{u}_k$ with $1 \leq k \leq m$ and $t \in \mathbb{R}$. Denote by Δ the matrix with Δ_k as columns. Then, as one moves from \mathbf{y} in the latent space in the direction of \mathbf{u}_k , the generated data changes by

$$\psi(\mathbf{y} + t\mathbf{u}_k) - \psi(\mathbf{y}) = t\Delta_k + \mathcal{O}(t^2).$$

Consider now a different direction, i.e., $k \neq k'$, and recall that \mathbf{u}_k and $\mathbf{u}_{k'}$ are orthogonal. A disentangled representation would satisfy: $\Delta_k^{\top} \Delta_{k'} = 0$. In other words, as the latent point moves along \mathbf{u}_k or along $\mathbf{u}_{k'}$, the decoder output varies in a significantly different manner. *Hence, for all \mathbf{y} in the latent space, we expect the Gram matrix $\Delta^{\top} \Delta$ to be diagonal.* To isolate the connection between the equation in Lemma 1 and the disentanglement of the representation, we assume that the encoder is already mapping points in the

³In [28], the constraint on U is implemented as a soft penalty term.

subspace defined by U , i.e., $\mathbf{y}_i = UU^\top \phi_\theta(\mathbf{x}_i) \approx \phi_\theta(\mathbf{x}_i)$ for all $1 \leq i \leq n$. From Lemma 1, we observe that the stochastic AE objective includes diagonalization terms involving the trace of a symmetric matrix. Then, we rely on Proposition 1 whose proof is straightforward.

Proposition 1 *Let M be a $\ell \times \ell$ symmetric matrix with distinct eigenvalues. Let ν_1, \dots, ν_m be its m smallest eigenvalues, with the associated eigenvectors $\mathbf{v}_1, \dots, \mathbf{v}_m$. Let V be the matrix whose columns are these eigenvectors. Then, the optimization problem $\min_{U \in \text{St}(\ell, m)} \text{Tr}(U^\top MU)$ is solved by $U^* = V$ and we have $U^{*\top} MU^* = \text{diag}(\boldsymbol{\nu})$, with $\boldsymbol{\nu} = (\nu_1, \dots, \nu_m)^\top$.*

If we consider only the second term in the equation in Lemma 1 and take $M_i = \nabla\psi(\mathbf{y}_i)\nabla\psi(\mathbf{y}_i)^\top$, we see, thanks to Proposition 1, that the optimization over $U \in \text{St}(\ell, m)$ promotes a diagonal Gram matrix $\Delta^\top \Delta = U^\top M_i U$. By construction, the loss (3) does not include the third term in the equation in Lemma 1. This motivated the introduction of the splitted loss. We now discuss the connections with probabilistic models and the independence of latent factors.

4 Connections with the Evidence Lower Bound

In order to formulate an ELBO for our proposed model, consider the following random encoders:

$$q(\mathbf{z}|\mathbf{x}) = \mathcal{N}(\mathbf{z}|\phi_\theta(\mathbf{x}), \gamma^2 \mathbb{I}_\ell) \text{ and } q_U(\mathbf{z}|\mathbf{x}) = \mathcal{N}(\mathbf{z}|\mathbb{P}_U \phi_\theta(\mathbf{x}), \sigma^2 \mathbb{P}_U + \delta^2 \mathbb{P}_{U^\perp}),$$

where ϕ_θ has zero mean on the data distribution. Here, σ^2 plays the role of a trade-off parameter, while the regularization parameter δ is introduced for technical reasons and is put to a numerically small absolute value (see supplementary material for details). Let the decoder be $p(\mathbf{x}|\mathbf{z}) = \mathcal{N}(\mathbf{x}|\psi_\xi(\mathbf{z}), \sigma_0^2 \mathbb{I})$ and the latent space distribution is parametrized by $p(\mathbf{z}) = \mathcal{N}(0, \Sigma)$ where $\Sigma \in \mathbb{R}^{\ell \times \ell}$ is a covariance matrix. We treat Σ as a parameter of the optimization problem that is determined at the last stage of the training. Then the minimization problem (St-RKM) with stochastic AE loss is equivalent to the maximization of

$$\frac{1}{n} \sum_{i=1}^n \left\{ \underbrace{\mathbb{E}_{q_U(\mathbf{z}|\mathbf{x}_i)}[\log(p(\mathbf{x}_i|\mathbf{z}))]}_{(I)} - \underbrace{\text{KL}(q_U(\mathbf{z}|\mathbf{x}_i), q(\mathbf{z}|\mathbf{x}_i))}_{(II)} - \underbrace{\text{KL}(q_U(\mathbf{z}|\mathbf{x}_i), p(\mathbf{z}))}_{(III)} \right\}, \quad (5)$$

which is a lower bound to the ELBO, since the KL divergence in (II) is positive. The hyper-parameters γ, σ, σ_0 take a fixed value. Up to additive constants, the terms (I) and (II) of (5) match the objective (St-RKM). The third term (III) in (5) is optimized after the training of the first two terms. It can be written as follows

$$\frac{1}{n} \sum_{i=1}^n \text{KL}(q_U(\mathbf{z}|\mathbf{x}_i), p(\mathbf{z})) = \frac{1}{2} \text{Tr}[\Sigma_0 \Sigma^{-1}] + \frac{1}{2} \log(\det \Sigma) + \text{constants}$$

with $\Sigma_0 = \mathbb{P}_U C_\theta \mathbb{P}_U + \sigma^2 \mathbb{P}_U + \delta^2 \mathbb{P}_{U^\perp}$. Hence, in that case, the optimal covariance matrix is diagonalized $\Sigma = U(\text{diag}(\boldsymbol{\lambda}) + \sigma^2 \mathbb{I}_m)U^\top + \delta^2 \mathbb{P}_{U^\perp}$, with $\boldsymbol{\lambda}$ denoting the principal values of the PCA.

Now we briefly discuss the factorization of the encoder. Let $\mathbf{h}(\mathbf{x}) = U^\top \phi_\theta(\mathbf{x})$ and let the ‘effective’ latent variable be $\mathbf{z}^{(U)} = U^\top \mathbf{z} \in \mathbb{R}^m$. Then the probability density function of $q_U(\mathbf{z}|\mathbf{x})$ is

$$f_{q_U(\mathbf{z}|\mathbf{x})}(\mathbf{z}) = \frac{e^{-\frac{\|\mathbf{U}_\perp^\top \mathbf{z}\|_2^2}{2\delta^2}}}{(\sqrt{2\pi\delta^2})^{\ell-m}} \prod_{j=1}^m \frac{e^{-\frac{(\mathbf{z}_j^{(U)} - \mathbf{h}_j(\mathbf{x}))^2}{2\sigma^2}}}{\sqrt{2\pi\sigma^2}},$$

where the first factor is approximated by a Dirac delta if $\delta \rightarrow 0$. Hence, the factorized form of q_U indicates the independence of the latent variables $\mathbf{z}^{(U)}$. This independence has been argued to promote disentanglement. In particular, the term (II) in (5) is analogous to a ‘Total Correlation’ loss [6], although not formally equal.

5 Experiments

In this section, we investigate if St-RKM⁴ can simultaneously achieve (i) accurate reconstructions on training data (ii) good random generations, and (iii) good disentanglement performance. We use the standard datasets: MNIST [14], Fashion-MNIST [29] (fMNIST), and SVHN [21]. To evaluate disentanglement, we use datasets

⁴The source code is available at https://github.com/EigenPandey/Stiefel_Restricted_Kernel_Machine

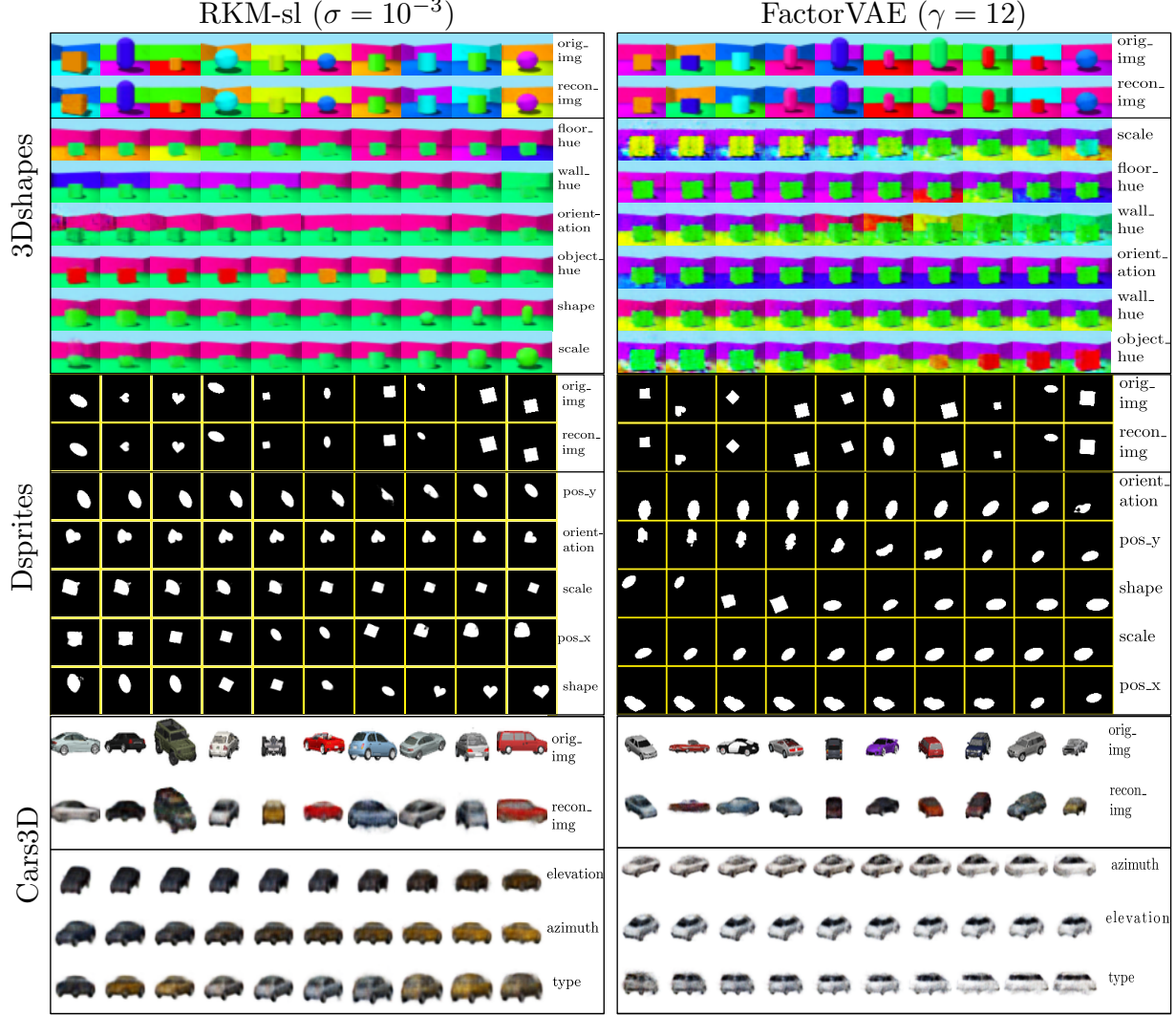


Figure 3: Traversals along principal components. First-two rows show the ground-truth and reconstructed images. Further each subsequent row show the generated images by traversing along a principal component in the latent space. The last column in each sub-image shows the dominant factor of variation.

with known ground-truth generating factors such as Dsprites [19], 3Dshapes [4], and Cars3D [24]. Further, all tables report average errors with 1 standard deviation over 10 experiments.

Algorithm: We use an alternating-minimization scheme (further described in supplementary material). First, the Adam optimizer with learning rate 2×10^{-4} is used to update the encoder-decoder parameters and then, the Cayley Adam optimizer [16] with learning rate 10^{-4} is used to update the U . Finally at the end of the training, we recompute U from the Singular Value Decomposition (SVD) of the covariance matrix as a final correction-step of the Kernel PCA term in our objective (step 10 of algorithm 1). Since the $\ell \times \ell$ covariance matrix is typically small, this decomposition is fast (see table 6). In practice, our training procedure only marginally increases the computation cost which can be seen from training times in Table 2.

Table 2: Training time in minutes (for 1000 epochs) and number of parameters of the generative models on MNIST dataset.

Model	St-RKM	β -VAE	FactorVAE	Info-GAN
Nb parameters	4164519	4165589	8182591	4713478
Training time	21.93 (± 1.3)	19.83 (± 0.8)	33.31 (± 2.7)	45.96 (± 1.6)

Algorithm 1 Manifold optimization of St-RKM**Input:** $\{\mathbf{x}_i\}_{i=1}^n, \phi_{\theta}, \psi_{\zeta}, \mathcal{J} := \text{Eq. } St - RKM$ **Output:** Learned θ, ζ, U

```

1: procedure TRAIN
2:   while not converged do
3:      $\{\mathbf{x}\} \leftarrow \{\text{Get mini-batch}\}$ 
4:     Get embeddings  $\phi_{\theta}(\mathbf{x}) \leftarrow \mathbf{x}$ 
5:     Compute centered  $C_{\theta}$  ▷ Covariance matrix
6:     Update  $\{\theta_e, \psi_g\} \leftarrow \text{Adam}(\mathcal{J})$  ▷ Optimization step
7:     Update  $\{U\} \leftarrow \text{Cayley-Adam}(\mathcal{J})$  ▷ Optimization step
8:   end while
9:   Do steps 4-5 over whole dataset
10:   $U \leftarrow \text{SVD}(C_{\theta})$ 
11: end procedure

```

Table 3: Sliced Wasserstein Distance (SWD) evaluates the quality of randomly generated 8000 samples over 10 iterations (smaller is better). The multi-scale statistical similarity between distributions of local image patches drawn from the Laplacian pyramid is evaluated using the SWD. A small Wasserstein distance indicates that the distribution of the patches is similar, thus real and fake images appear similar in both appearance and variation at this spatial resolution. We always show the average SWD to evaluate performance. Scores are multiplied by 10^2 for better readability.

Models	MNIST	fMNIST	SVHN	3Dshapes	DSprites	Cars3D
St-RKM ($\sigma = 0$)	4.80 (± 0.13)	4.71 (± 0.14)	4.36 (± 0.32)	2.52 (± 0.18)	4.54 (± 0.64)	3.69 (± 1.4)
St-RKM ($\sigma = 10^{-3}$)	4.77 (± 0.12)	6.46 (± 0.17)	3.26 (± 0.16)	1.04 (± 0.14)	3.72 (± 0.58)	3.62 (± 1.29)
St-RKM-sl ($\sigma = 10^{-3}$)	3.11 (± 0.10)	5.17 (± 0.10)	4.16 (± 0.23)	1.20 (± 0.19)	3.13 (± 0.54)	4.02 (± 1.40)
VAE ($\beta = 1$)	4.85 (± 0.48)	5.60 (± 0.09)	4.50 (± 0.34)	2.06 (± 0.13)	5.04 (± 0.92)	4.01 (± 1.90)
β -VAE ($\beta = 3$)	3.75 (± 0.08)	7.16 (± 0.28)	4.71 (± 0.27)	3.25 (± 0.27)	4.85 (± 0.68)	4.83 (± 0.21)
FactorVAE ($\gamma = 12$)	3.52 (± 0.27)	5.12 (± 0.01)	3.46 (± 0.64)	1.32 (± 0.01)	3.24 (± 0.02)	3.47 (± 0.07)
InfoGAN	4.08 (± 0.27)	5.21 (± 1.33)	4.84 (± 0.72)	2.33 (± 0.36)	5.17 (± 0.31)	4.92 (± 0.33)

Experimental setup: We consider four baselines for comparison: (i) VAE, (ii) β -VAE, (iii) FactorVAE and (iv) Info-GAN. To be consistent in evaluation, we keep the same encoder (discriminator) and decoder (generator) architecture; and the same latent dimension across the models. In the case of Info-GAN, batch-normalization is added for training stability. For the determination of the hyperparameters of other methods, we start from values in the range of the parameters suggested in the authors' reference implementation. After trying various values we noticed that $\beta = 3$ and $\gamma = 12$ seem to work well across the datasets that we considered for β -VAE and FactorVAE respectively. Furthermore, in all experiments on St-RKM, we keep reconstruction weight $\lambda = 1$. All models are trained on the entire dataset. Further technical details are given in supplementary material. Note that for the same encoder-decoder network, the St-RKM model has the least number of parameters compared to any VAE variants and Info-GAN (see Table 2). To evaluate the quality of generated samples, we report the Fréchet Inception Distance [9] (FID) scores in Table 1 and the Sliced Wasserstein Distance (SWD) [11] scores in Table 3. Note that FID scores are not necessarily appropriate for Dsprites since this dataset is significantly different from ImageNet on which the Inception network was originally trained. Randomly generated samples are shown in Figure 4. To generate samples from deterministic St-RKM ($\sigma = 0$), we sample from a fitted normal distribution on the latent embeddings of the dataset (similar to [8]). St-RKM variants (shaded background) perform better on most datasets and within them, the stochastic variants with $\sigma = 10^{-3}$ performs the best. This can be attributed to a better generalization of the decoder network due to the addition of noise-term on latent-variables (see Lemma 1). The training times for St-RKM variants are shorter compared to FactorVAE and Info-GAN due to a significantly smaller number of parameters.

To evaluate the disentanglement performance, various metrics have been proposed. A comprehensive review by Locatello et al. [17] shows that the various disentanglement metrics are correlated albeit with a different degree of correlation across datasets. In this paper, we use three measures given in Eastwood's framework [7]: *disentanglement*: the degree to which a representation factorizes the underlying factors of variation, with each variable capturing at most one generative factor; *completeness*: the degree to which each underlying factor is captured by a single code variable; and *informativeness*: the amount of information that a representation captures about the underlying factors of variation. Table 4 shows that St-RKM variants (shaded background)

Table 4: Eastwood framework’s [7] disentanglement metric with Lasso and Random Forest regressor. For disentanglement and completeness higher score is better, for informativeness, lower is better. ‘Info.’ indicates (average) root-mean-square error in predicting z . The best scores are in bold. St-RKM variants are shaded and outperform other models except in two instances.

Dataset	Model	Lasso			Random Forest		
		Dise.	Comp.	Info.	Dise.	Comp.	Info.
Dsprites	St-RKM ($\sigma = 0$)	0.41 (± 0.02)	0.45 (± 0.01)	1.05 (± 0.03)	0.27 (± 0.01)	0.62 (± 0.01)	0.97 (± 0.03)
	St-RKM ($\sigma = 10^{-3}$)	0.45 (± 0.01)	0.47 (± 0.02)	1.05 (± 0.01)	0.28 (± 0.01)	0.63 (± 0.02)	1.02 (± 0.01)
	St-RKM-sl ($\sigma = 10^{-3}$)	0.37 (± 0.03)	0.32 (± 0.01)	1.07 (± 0.02)	0.35 (± 0.02)	0.58 (± 0.01)	0.96 (± 0.02)
	VAE ($\beta = 1$)	0.26 (± 0.06)	0.22 (± 0.00)	0.97 (± 0.01)	0.24 (± 0.03)	0.55 (± 0.04)	1.00 (± 0.01)
	β -VAE ($\beta = 3$)	0.36 (± 0.02)	0.31 (± 0.02)	0.96 (± 0.21)	0.33 (± 0.01)	0.53 (± 0.04)	0.99 (± 0.11)
	FactorVAE ($\gamma = 12$)	0.40 (± 0.01)	0.34 (± 0.01)	0.98 (± 0.01)	0.34 (± 0.02)	0.58 (± 0.01)	1.05 (± 0.01)
	Info-GAN	0.31 (± 0.21)	0.27 (± 0.03)	0.95 (± 0.02)	0.31 (± 0.01)	0.47 (± 0.20)	1.00 (± 0.02)
3Dshapes	St-RKM ($\sigma = 0$)	0.76 (± 0.02)	0.71 (± 0.02)	1.06 (± 0.03)	0.55 (± 0.03)	0.69 (± 0.02)	0.51 (± 0.21)
	St-RKM ($\sigma = 10^{-3}$)	0.74 (± 0.02)	0.66 (± 0.01)	1.24 (± 0.02)	0.61 (± 0.01)	0.67 (± 0.01)	0.86 (± 0.10)
	St-RKM-sl ($\sigma = 10^{-3}$)	0.72 (± 0.01)	0.65 (± 0.01)	1.03 (± 0.02)	0.63 (± 0.02)	0.66 (± 0.02)	0.95 (± 0.01)
	VAE ($\beta = 1$)	0.44 (± 0.21)	0.33 (± 0.22)	1.26 (± 0.20)	0.33 (± 0.20)	0.36 (± 0.21)	0.94 (± 0.01)
	β -VAE ($\beta = 3$)	0.55 (± 0.01)	0.54 (± 0.01)	1.07 (± 0.01)	0.56 (± 0.01)	0.57 (± 0.03)	0.54 (± 0.22)
	FactorVAE ($\gamma = 12$)	0.62 (± 0.01)	0.41 (± 0.03)	1.05 (± 0.01)	0.57 (± 0.02)	0.58 (± 0.01)	0.93 (± 0.20)
	Info-GAN	0.41 (± 0.22)	0.39 (± 0.01)	1.17 (± 0.02)	0.53 (± 0.01)	0.51 (± 0.10)	0.61 (± 0.12)
Cars3D	St-RKM ($\sigma = 0$)	0.45 (± 0.01)	0.27 (± 0.13)	1.33 (± 0.08)	0.49 (± 0.01)	0.38 (± 0.01)	1.16 (± 0.03)
	St-RKM ($\sigma = 10^{-3}$)	0.42 (± 0.09)	0.40 (± 0.02)	1.34 (± 0.03)	0.54 (± 0.01)	0.32 (± 0.02)	1.20 (± 0.11)
	St-RKM-sl ($\sigma = 10^{-3}$)	0.63 (± 0.02)	0.48 (± 0.01)	1.30 (± 0.05)	0.55 (± 0.02)	0.33 (± 0.02)	1.20 (± 0.03)
	VAE ($\beta = 1$)	0.47 (± 0.01)	0.18 (± 0.04)	1.34 (± 0.02)	0.23 (± 0.21)	0.35 (± 0.01)	1.21 (± 0.02)
	β -VAE ($\beta = 3$)	0.51 (± 0.06)	0.27 (± 0.08)	1.35 (± 0.01)	0.47 (± 0.07)	0.37 (± 0.02)	1.19 (± 0.07)
	FactorVAE ($\gamma = 12$)	0.54 (± 0.02)	0.38 (± 0.23)	1.33 (± 0.02)	0.44 (± 0.01)	0.33 (± 0.01)	1.24 (± 0.01)
	Info-GAN	0.56 (± 0.01)	0.23 (± 0.13)	1.29 (± 0.04)	0.27 (± 0.22)	0.32 (± 0.05)	1.41 (± 0.21)

have better disentanglement and completeness scores. However, informativeness scores are higher for St-RKM when using a lasso-regressor in contrast to mixed scores with Random forest regressor. This can be seen clearly in Figure 3 which shows the generated images by traversing along the principal components in the latent space. In 3Dshapes dataset, St-RKM model captures floor-hue, wall-hue, and orientation perfectly but has a slight entanglement in capturing other factors. This is worse in β -VAE which has entanglement in all dimensions except the floor-hue along with noise in some generated images. Similar trends can be observed in the Dsprites and Cars3D dataset.

6 Related work

VAE: It has been shown in [6] that the KL term includes the Mutual Information Gap which encourages disentanglement. In [5], the effect of the β term is analyzed more in-depth. It was suggested that the stronger emphasis on the posterior to match the factorized unit Gaussian prior puts further constraints on the implicit capacity of the latent bottleneck [10]. Recently, several variants of VAEs promoting disentanglement have been proposed by adding extra terms to the ELBO. For instance, FactorVAE [12] augments the ELBO by a new term enforcing factorization of the marginal posterior (or aggregate posterior). The work of [18] considers adding an extra term that accounts for the knowledge of some partial label information to improve disentanglement. In [26] the reason for the alignment of the latent space with the coordinate axes is analyzed, as the design of VAE does not suggest any such mechanism. The authors argue that due to the diagonal approximation in the encoder together with the inherent stochasticity forces the local orthogonality of the decoder. In contrast to [26] where the implicit orthogonality of VAE is studied, our proposed model has orthogonality by design due to the introduction of the Stiefel manifold. The use of deterministic AEs was studied in [8], where another quadratic regularization on the latent vectors was proposed.

RKM: In [23, 22] for instance, a multi-view generative model called Generative-RKM (Gen-RKM) has been introduced which uses explicit feature-maps in a novel training procedure for joint feature-selection and subspace learning.

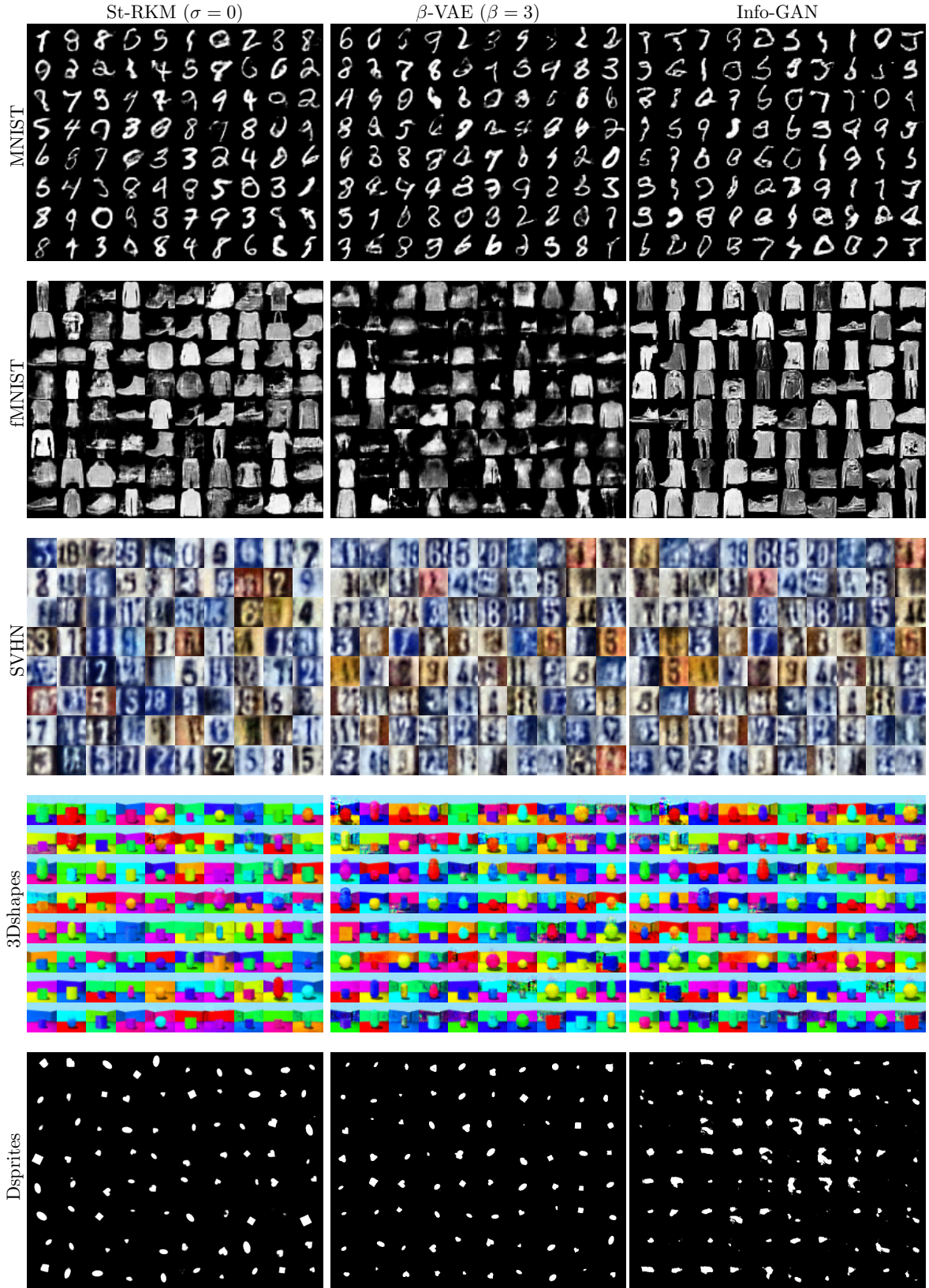


Figure 4: Samples of randomly generated batch of images used to compute FID scores (see Table 1 in main part) and SWD scores (see Table 3).

7 Conclusion

We proposed two main changes with respect to related works: (i) In contrast with [23], the interconnection matrix U is restricted to be a rectangular matrix with orthonormal columns, i.e., valued on a Stiefel manifold. Then, for the training, we use the Cayley Adam algorithm of [16] for stochastic optimization on the Stiefel manifold. Computationally, St-RKM only increases the training time by a reasonably small amount compared to β -VAE for instance. (ii) We propose several Auto-Encoder objectives and discuss that the combination of a stochastic AE loss with an explicit optimization on the Stiefel manifold promotes disentanglement. (iii) Additionally, we establish connections with probabilistic models, formulate an Evidence Lower Bound (ELBO), and discuss the independence of latent factors. Where the considered baselines have a trade-off between generation quality and disentanglement, we improve on both these aspects as illustrated through various experiments.

Acknowledgments

EU: The research leading to these results has received funding from the European Research Council under the European Union's Horizon 2020 research and innovation program / ERC Advanced Grant E-DUALITY (787960). This paper reflects only the authors' views and the Union is not liable for any use that may be made of the contained information. Research Council KUL: Optimization frameworks for deep kernel machines C14/18/068 Flemish Government: FWO: projects: GOA4917N (Deep Restricted Kernel Machines: Methods and Foundations), PhD/Postdoc grant Impulsfonds AI: VR 2019 2203 DOC.0318/1QUATER Kenniscentrum Data en Maatschappij This research received funding from the Flemish Government (AI Research Program). The authors are affiliated to Leuven.AI - KU Leuven institute for AI, B-3000, Leuven, Belgium. Ford KU Leuven Research Alliance Project KUL0076 (Stability analysis and performance improvement of deep reinforcement learning algorithms(s), ICT 48 TAILOR, Leuven.AI Institute. The computational resources and services used in this work were provided by the VSC (Flemish Supercomputer Center), funded by the Research Foundation - Flanders (FWO) and the Flemish Government – department EWI.

A Proof of Lemma 3.1

We first quote a result that is used in the context of optimization ([20], Lemma 1.2.4). Let f a function with L -Lipschitz continuous Hessian. Then, it holds

$$\underbrace{\left| f(\mathbf{y}_1) - f(\mathbf{y}) - \nabla f(\mathbf{y})^\top (\mathbf{y}_1 - \mathbf{y}) - \frac{1}{2}(\mathbf{y}_1 - \mathbf{y})^\top \text{Hess}_{\mathbf{y}}[f](\mathbf{y}_1 - \mathbf{y}) \right|}_{r(\mathbf{y}_1 - \mathbf{y})} \leq \frac{L}{6} \|\mathbf{y}_1 - \mathbf{y}\|_2^3. \quad (6)$$

Then, we calculate the power series expansion of $f(\mathbf{y}) = [\mathbf{x} - \boldsymbol{\psi}(\mathbf{y})]_a^2$ and take the expectation with respect to $\boldsymbol{\epsilon} \sim \mathcal{N}(0, \mathbb{I})$. Firstly, we have

$$\nabla f(\mathbf{y}) = -2[\mathbf{x} - \boldsymbol{\psi}(\mathbf{y})]_a \nabla \boldsymbol{\psi}_a(\mathbf{y})$$

and

$$\text{Hess}_{\mathbf{y}}[f] = 2\nabla \boldsymbol{\psi}_a(\mathbf{y}) \nabla \boldsymbol{\psi}_a(\mathbf{y})^\top - 2[\mathbf{x} - \boldsymbol{\psi}(\mathbf{y})]_a \text{Hess}_{\mathbf{y}}[\boldsymbol{\psi}_a].$$

Then, we use (6) with $\mathbf{y}_1 - \mathbf{y} = \sigma U \boldsymbol{\epsilon}$. By taking the expectation over $\boldsymbol{\epsilon}$, notice that the order 1 term in σ vanishes since $\mathbb{E}_{\boldsymbol{\epsilon}}[\boldsymbol{\epsilon}] = 0$. We find

$$\begin{aligned} \mathbb{E}_{\boldsymbol{\epsilon}}[\mathbf{x} - \boldsymbol{\psi}(\mathbf{y} + \sigma U \boldsymbol{\epsilon})]_a^2 &= [\mathbf{x} - \boldsymbol{\psi}(\mathbf{y})]_a^2 + \sigma^2 \text{Tr}(U^\top \nabla \boldsymbol{\psi}_a(\mathbf{y}) \nabla \boldsymbol{\psi}_a(\mathbf{y})^\top U) \\ &\quad - \sigma^2 [\mathbf{x} - \boldsymbol{\psi}(\mathbf{y})]_a \text{Tr}(U^\top \text{Hess}_{\mathbf{y}}[\boldsymbol{\psi}_a] U) + \mathbb{E}_{\boldsymbol{\epsilon}} r(\sigma U \boldsymbol{\epsilon}), \end{aligned}$$

where we used that $\mathbb{E}_{\boldsymbol{\epsilon}}[\boldsymbol{\epsilon}^\top M \boldsymbol{\epsilon}] = \text{Tr}[M]$ for any symmetric matrix M since $\mathbb{E}_{\boldsymbol{\epsilon}}[\boldsymbol{\epsilon}_i \boldsymbol{\epsilon}_j] = \delta_{ij}$. Next, denote $R_a(\sigma) = \mathbb{E}_{\boldsymbol{\epsilon}} r(\sigma U \boldsymbol{\epsilon})$ we can use the Jensen inequality and subsequently (6)

$$|R_a(\sigma)| = |\mathbb{E}_{\boldsymbol{\epsilon}} r(\sigma U \boldsymbol{\epsilon})| \leq \mathbb{E}_{\boldsymbol{\epsilon}} |r(\sigma U \boldsymbol{\epsilon})| \leq \frac{L}{6} \mathbb{E}_{\boldsymbol{\epsilon}} \|\sigma U \boldsymbol{\epsilon}\|_2^3.$$

Next, we notice that $\|\sigma U \boldsymbol{\epsilon}\|_2 = \sigma(\boldsymbol{\epsilon}^\top U^\top U \boldsymbol{\epsilon})^{1/2} = \sigma\|\boldsymbol{\epsilon}\|_2$. It is useful to notice that $\|\boldsymbol{\epsilon}\|_2$ is distributed according to a chi distribution. By using this remark, we find

$$|R_a(\sigma)| \leq \sigma^3 \frac{L}{6} \mathbb{E}_{\boldsymbol{\epsilon}} \|\boldsymbol{\epsilon}\|_2^3 = \sigma^3 \frac{L}{6} \frac{\sqrt{2}(m+1)\Gamma((m+1)/2)}{\Gamma(m/2)},$$

where the last equality uses the expression for the third moment of the chi distribution and where the Gamma function Γ is the extension of the factorial to the complex numbers.

B Details on Evidence Lower Bound for St-RKM model

We discuss here the details of the ELBO given in section 4. The first term in (4.4) is

$$\mathbb{E}_{q_U(\mathbf{z}|\mathbf{x}_i)}[\log(p(\mathbf{x}_i|\mathbf{z}))] = \frac{1}{2\sigma_0^2} \mathbb{E}_{\epsilon \sim \mathcal{N}(0, \mathbb{I})} \|\mathbf{x}_i - \psi_{\xi}(\mathbb{P}_U \phi_{\theta}(\mathbf{x}_i) + \sigma \mathbb{P}_U \epsilon + \delta \mathbb{P}_{U^\perp} \epsilon)\|_2^2 - \frac{d}{2} \log(2\pi\sigma_0^2).$$

Clearly, the above expectation can be written as follows

$$\mathbb{E}_{\epsilon} \mathbb{E}_{\epsilon^\perp} \|\mathbf{x}_i - \psi_{\xi}(\mathbb{P}_U \phi_{\theta}(\mathbf{x}_i) + \sigma U \epsilon + \delta U^\perp \epsilon^\perp)\|_2^2,$$

with $\epsilon \sim \mathcal{N}(0, \mathbb{I}_m)$ and $\epsilon^\perp \sim \mathcal{N}(0, \mathbb{I}_{\ell-m})$. Hence, we fix $\sigma_0^2 = 1/2$ and take $\delta > 0$ to a numerically small value. For the other terms of (4.4), we use the formula giving the KL divergence between multivariate normals. Let \mathcal{N}_0 and \mathcal{N}_1 be ℓ -variate normal distributions with mean μ_0, μ_1 and covariance Σ_0, Σ_1 respectively. Then,

$$\text{KL}(\mathcal{N}_0, \mathcal{N}_1) = \frac{1}{2} \left\{ \text{Tr}(\Sigma_1^{-1} \Sigma_0) + (\mu_1 - \mu_0)^\top \Sigma_1^{-1} (\mu_1 - \mu_0) - \ell + \log \left(\frac{\det \Sigma_1}{\det \Sigma_0} \right) \right\}$$

By using this identity, we find the second term of (4.4):

$$\begin{aligned} \text{KL}[q_U(\mathbf{z}|\mathbf{x}_i), q(\mathbf{z}|\mathbf{x}_i)] &= \frac{1}{2} \left\{ \frac{m\sigma^2 + (\ell - m)\delta^2}{\gamma^2} + \frac{1}{\gamma^2} \|\phi_{\theta}(\mathbf{x}_i) - \mathbb{P}_U \phi_{\theta}(\mathbf{x}_i)\|_2^2 \right. \\ &\quad \left. - \ell + \log \left(\frac{\gamma^{2\ell}}{\sigma^{2k} \delta^{2(\ell-m)}} \right) \right\}. \end{aligned}$$

For the third term in (4.4), we find

$$\begin{aligned} \text{KL}[q_U(\mathbf{z}|\mathbf{x}_i), p(\mathbf{z})] &= \frac{1}{2} \left\{ \text{Tr}((\sigma^2 \mathbb{P}_U + \delta^2 \mathbb{P}_{U^\perp}) \Sigma^{-1}) + (\mathbb{P}_U \phi_{\theta}(\mathbf{x}_i))^\top \Sigma^{-1} (\mathbb{P}_U \phi_{\theta}(\mathbf{x}_i)) \right. \\ &\quad \left. + \log \det(\Sigma) - \ell - \log(\sigma^{2m} \delta^{2(\ell-m)}) \right\}. \end{aligned}$$

By averaging over $i = 1, \dots, n$, we obtain

$$\begin{aligned} \frac{1}{n} \sum_{i=1}^n \text{KL}[q_U(\mathbf{z}|\mathbf{x}_i), p(\mathbf{z})] &= \frac{1}{2} \left\{ \text{Tr}((\sigma^2 \mathbb{P}_U + \delta^2 \mathbb{P}_{U^\perp}) \Sigma^{-1}) + \text{Tr}(\mathbb{P}_U C_{\theta} \mathbb{P}_U \Sigma^{-1}) \right. \\ &\quad \left. + \log \det(\Sigma) - \ell - \log(\sigma^{2m} \delta^{2(\ell-m)}) \right\}, \end{aligned}$$

where we used the cyclic property of the trace and $C_{\theta} = \frac{1}{n} \sum_{i=1}^n \phi_{\theta}(\mathbf{x}_i) \phi_{\theta}(\mathbf{x}_i)^\top$. This proves the analogous expression in section 4. Finally, the estimation of the optimal Σ can be done in parallel to the Maximum Likelihood Estimation of the covariance matrix of a multivariate normal.

C Analysis of St-RKM with a fixed U (an ablation study)

We discuss here the role of the optimization of $\text{St}(\ell, m)$ on disentanglement in the case of a classical AE loss ($\sigma = 0$). To do so, a matrix $\tilde{U} \in \text{St}(\ell, m)$ is generated randomly⁵ and kept fixed during the training of the following optimization problem

$$\min_{\theta, \xi} \lambda \frac{1}{n} \sum_{i=1}^n L_{\xi, \tilde{U}}^{(0)}(\mathbf{x}_i, \phi_{\theta}(\mathbf{x}_i)) + \underbrace{\frac{1}{n} \sum_{i=1}^n \|\mathbb{P}_{\tilde{U}^\perp}^{(\varepsilon)} \phi_{\theta}(\mathbf{x}_i)\|_2^2}_{\text{regularized PCA objective}} \quad (7)$$

with $\lambda = 1$ and where $\varepsilon \geq 0$ is a regularization constant and where the regularized (or mollified) projector $\mathbb{P}_{\tilde{U}^\perp}^{(\varepsilon)} = \varepsilon(\tilde{U}\tilde{U}^\top + \varepsilon\mathbb{I}_{\ell})^{-1}$ is used in order to prevent numerical instabilities. Indeed, if $\varepsilon = 0$, the second term in (7) (PCA term) is not strictly convex as a function of ϕ_{θ} , since this quadratic form has flat directions along the column subspace of \tilde{U} . Our numerical simulations in single precision pytorch with $\varepsilon = 0$ exhibit instabilities, i.e., the PCA term in (7) takes negative values during the training. Hence, the regularized projector is introduced so that the PCA quadratic is strongly convex for $\varepsilon > 0$. This instability is not observed in the training of (St-RKM) where U is not fixed. This is one asset of our training procedure using optimization over Stiefel manifold. Explicitly, the regularized projector satisfies the following properties

- $\mathbb{P}_{\tilde{U}^\perp}^{(\varepsilon)} u_{\perp} = u_{\perp}$ for all $u_{\perp} \in (\text{range}(U))^\perp$,

⁵Using a random $\tilde{U} \in \text{St}(\ell, m)$ can be interpreted as sketching the encoder map in the spirit of Randomized Orthogonal Systems (ROS) sketches (see [30]).

- $\mathbb{P}_{\tilde{U}^\perp}^{(\varepsilon)} u = \varepsilon u$ for all $u \in \text{range}(U)$.

Clearly, thanks to the push-through identity, we have the alternative expression $\mathbb{P}_{\tilde{U}^\perp}^{(\varepsilon)} = \mathbb{I} - U(U^\top U + \varepsilon \mathbb{I}_m)^{-1} U^\top$. Therefore, it holds $\lim_{\varepsilon \rightarrow 0} \mathbb{P}_{\tilde{U}^\perp}^{(\varepsilon)} = \mathbb{P}_{\tilde{U}^\perp}$, as it should. In our experiments, we set $\varepsilon = 10^{-5}$. If $\varepsilon \leq 10^{-6}$, the regularized PCA objective in (7) takes negative values after a few epochs due to the numerical instability as mentioned above.

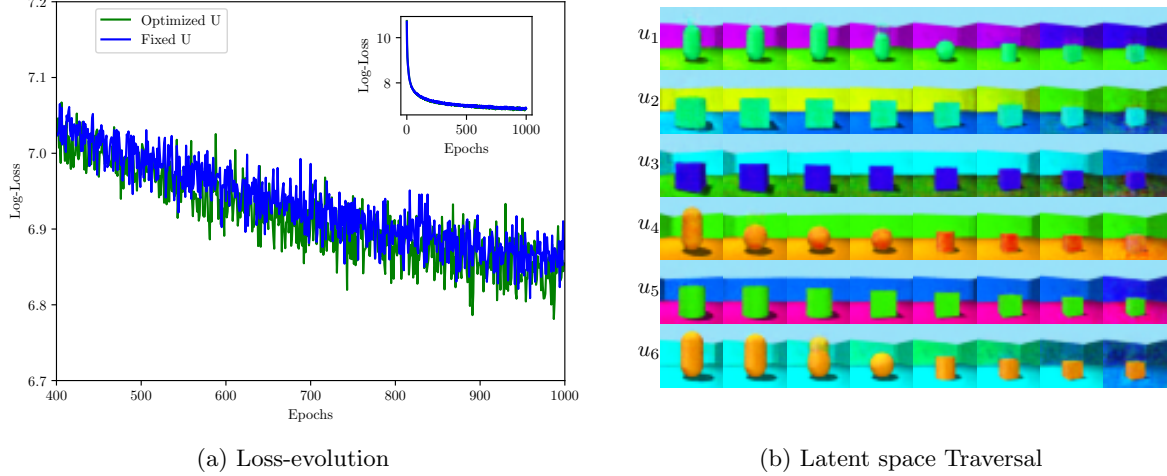


Figure 5: (a) Loss evolution (log plot) during the training of (7) over 1000 epochs with $\varepsilon = 10^{-5}$ once with Cayley-Adam optimizer (green curve) and then without (blue curve). (b) Traversals along the principal components when the model was trained with a fixed U , i.e. with the objective given by (7) and $\varepsilon = 10^{-5}$. There is no clear isolation of a feature along any of the principal components indicating further that optimizing over U is key for better disentanglement.

In Figure 5a, the evolution of the training objective (7) is displayed. It can be seen that the final objective has lower value [$\exp(6.78) \approx 881$] when U is optimized compared to its fixed counterpart [$\exp(6.81) \approx 905$] showing the merit of optimizing over Stiefel manifold for the same parameter ε . Hence, the subspace determined by $\text{range}(U)$ has to be adapted to the encoder and decoder networks. In other words, the training over θ, ξ is not sufficient to minimize the $\text{St}(\ell, m)$ objective with Adam. Figure 5b further explores the latent traversals in context of this ablation study. In the top row of Figure 5b (latent traversal in the direction of u_1), both the shape of the object and the wall hue are changing. A coupling between wall hue and shape is also visible in the bottom row of this figure.

D Datasets, Hyperparameters and Algorithm

We refer to Table 5 and Table 6 for more details on model architectures, datasets and hyperparameters used in this paper. All models were trained on full-datasets and for maximum 1000 epochs. Further all datasets are scaled between [0-1] and are resized to 28×28 dimensions except Dsprites and Cars3D. The PyTorch library (single precision) in Python was used as the programming language on 8GB NVIDIA QUADRO P4000 GPU. See Algorithm 1 for training the St-RKM model. In the case of FactorVAE, the discriminator architecture is same as proposed in the original paper [12].

Table 5: Datasets and hyperparameters used for the experiments. N is the number of training samples, d the input dimension (resized images), m the subspace dimension and M the minibatch size.

Dataset	N	d	m	M
MNIST	60000	28×28	10	256
fMNIST	60000	28×28	10	256
SVHN	73257	$32 \times 32 \times 3$	10	256
Dsprites	737280	64×64	5	256
3Dshapes	480000	$64 \times 64 \times 3$	6	256
Cars3D	17664	$64 \times 64 \times 3$	3	256

Table 6: Model architectures. All convolutions and transposed-convolutions are with stride 2 and padding 1. Unless stated otherwise, layers have Parametric-RELU ($\alpha = 0.2$) activation functions, except output layers of the pre-image maps which have sigmoid activation functions (since input data is normalized $[0, 1]$). Adam and Cayley Adam optimizers have learning rates 2×10^{-4} and 10^{-4} respectively. Pre-image map/decoder network is always taken as transposed of feature-map/encoder network. $c = 48$ for Cars3D; and $c = 64$ for all others. Further, $\hat{k} = 3$ and stride 1 for MNIST, fMNIST, SVHN and 3Dshapes; and $\hat{k} = 4$ for others. SVHN and 3Dshapes are resized to 28×28 input dimensions.

Dataset	Architecture
MNIST/fMNIST/ /SVHN/3Dshapes/ Dsprites/Cars3D	$\phi_\theta(\cdot) = \begin{cases} Conv [c] \times 4 \times 4; \\ Conv [c \times 2] \times 4 \times 4; \\ Conv [c \times 4] \times \hat{k} \times \hat{k}; \\ FC 256; \\ FC 50 (Linear) \end{cases}$ $\psi_\zeta(\cdot) = \begin{cases} FC 256; \\ FC [c \times 4] \times \hat{k} \times \hat{k}; \\ Conv [c \times 2] \times 4 \times 4; \\ Conv [c] \times 4 \times 4; \\ Conv [c] (Sigmoid) \end{cases}$

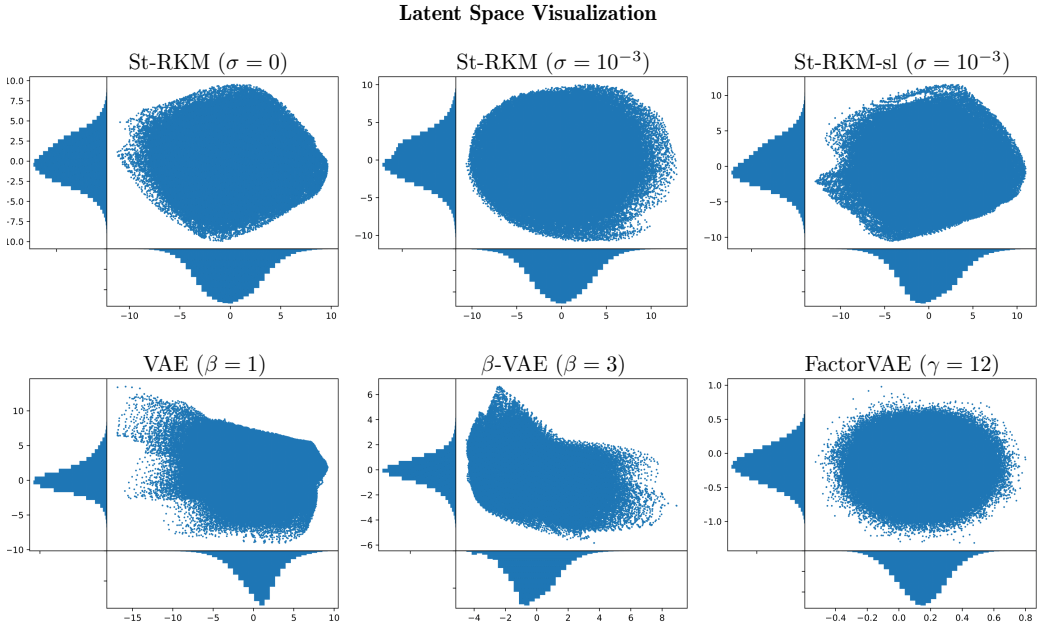


Figure 6: Scatter plots of latent variables with histograms. The models were trained on full Dsprites dataset (737280 points). In the case of St-RKMs, the joint distributions are always centered around zero and elliptically distributed.

E Additional Empirical Results

In Figure 6, a two dimensional projection of the embedding of the Dsprites data set in latent space is displayed. A successful optimization procedure is expected to yield a Gaussian cluster in feature space. Since random generation requires sampling from a latent normal distribution, the models which do not respect this constraint strongly are expected to generate poorer quality images (FID/SWD scores). This can be confirmed from the results in Table 1 and Table 3. Figure 7 reports the training curves of the models considered in this paper. This confirms that the models have been trained with a sufficiently large number of epochs.

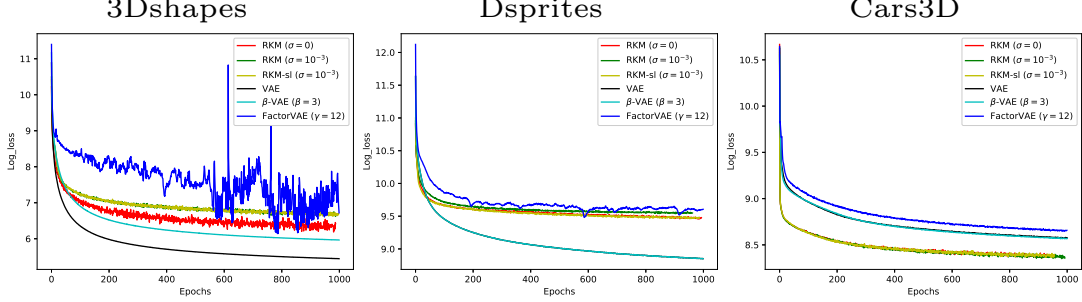


Figure 7: Reconstruction errors (log-scale) of various models during the training process over 1000 epochs, after which no significant improvement of the objectives can be observed. Further the final losses may not be compared in absolute sense since the models are different.

References

- [1] P.-A. Absil, R. Mahony, and R. Sepulchre. *Optimization Algorithms on Matrix Manifolds*. Princeton University Press, Princeton, NJ, 2008.
- [2] Haim Avron, Huy Nguyen, and David Woodruff. Subspace Embeddings for the Polynomial Kernel. In *Advances in Neural Information Processing Systems*, volume 27, pages 2258–2266, 2014.
- [3] Yoshua Bengio, Aaron Courville, and Pascal Vincent. Representation Learning: A Review and New Perspectives. *IEEE Transactions on Pattern Analysis and Machine Intelligence*, 35(8):1798–1828, 2013.
- [4] Chris Burgess and Hyunjik Kim. 3Dshapes Dataset. <https://github.com/deepmind/3dshapes-dataset/>, 2018.
- [5] Christopher P Burgess, Irina Higgins, Arka Pal, Loic Matthey, Nick Watters, Guillaume Desjardins, and Alexander Lerchner. Understanding disentangling in β -VAE. In *NIPS 2017 Workshop on Learning Disentangled Representations: from Perception to Control*, 2017.
- [6] Ricky T. Q. Chen, Xuechen Li, Roger B Grosse, and David K Duvenaud. Isolating Sources of Disentanglement in Variational Autoencoders. In *Advances in Neural Information Processing Systems 31*, pages 2610–2620, 2018.
- [7] Cian Eastwood and Christopher K. I. Williams. A Framework for the Quantitative Evaluation of Disentangled Representations. In *proceedings of the International Conference on Learning Representations (ICLR)*, 2018.
- [8] Partha Ghosh, Mehdi SM Sajjadi, Antonio Vergari, Michael Black, and Bernhard Schölkopf. From Variational to Deterministic Autoencoders. In *proceedings of the International Conference on Learning Representations (ICLR)*, 2020.
- [9] Martin Heusel, Hubert Ramsauer, Thomas Unterthiner, Bernhard Nessler, and Sepp Hochreiter. GANs Trained by a Two Time-scale Update Rule Converge to a Local Nash Equilibrium. In *Advances in Neural Information Processing Systems*, pages 6629–6640, 2017.
- [10] Irina Higgins, Loic Matthey, Arka Pal, Christopher Burgess, Xavier Glorot, Matthew Botvinick, Shakir Mohamed, and Alexander Lerchner. Beta-VAE: Learning Basic Visual Concepts with a Constrained Variational Framework. In *proceedings of the International Conference on Learning Representations (ICLR)*, volume 2, page 6, 2017.
- [11] Tero Karras, Timo Aila, Samuli Laine, and Jaakko Lehtinen. Progressive Growing of GANs for Improved Quality, Stability, and Variation. In *proceedings of the International Conference on Learning Representations (ICLR)*, 2017.
- [12] Hyunjik Kim and Andriy Mnih. Disentangling by Factorising. In *proceedings of the Thirty-fifth International Conference on Machine Learning (ICML)*, volume 80, pages 2649–2658, 2018.
- [13] Diederik P. Kingma and Max Welling. Auto-Encoding Variational Bayes. In *proceedings of the International Conference on Learning Representations (ICLR)*, 2014.
- [14] Yann LeCun and Corinna Cortes. MNIST handwritten digit database. <http://yann.lecun.com/exdb/mnist/>, 2010.
- [15] Yann LeCun, Fu Jie Huang, and Leon Bottou. Learning Methods for Generic Object Recognition with Invariance to Pose and Lighting. In *Computer Vision and Pattern Recognition (CVPR)*, volume 2, 2004.
- [16] Jun Li, Fuxin Li, and Sinisa Todorovic. Efficient Riemannian Optimization on the Stiefel Manifold via the Cayley Transform. In *proceedings of the International Conference on Learning Representations (ICLR)*, 2020.
- [17] Francesco Locatello, Stefan Bauer, Mario Lučić, Gunnar Rätsch, Sylvain Gelly, Bernhard Schölkopf, and Olivier Frederic Bachem. Challenging Common Assumptions in the Unsupervised Learning of Disentangled Representations. In *International Conference on Machine Learning (ICML)*, 2019.

- [18] Francesco Locatello, Michael Tschannen, Stefan Bauer, Gunnar Rätsch, Bernhard Schölkopf, and Olivier Bachem. Disentangling Factors of Variations Using Few Labels. In *International Conference on Learning Representations (ICLR)*, 2020.
- [19] Loic Matthey, Irina Higgins, Demis Hassabis, and Alexander Lerchner. dsprites: Disentanglement testing sprites dataset. <https://github.com/deepmind/dsprites-dataset/>, 2017.
- [20] Yurii Nesterov. *Introductory Lectures on Convex Optimization: A Basic Course*. Springer Publishing Company, Incorporated, 1st edition, 2014.
- [21] Yuval Netzer, Tao Wang, Adam Coates, Alessandro Bissacco, Bo Wu, and Andrew Y Ng. Reading Digits in Natural Images with Unsupervised Feature Learning. In *NIPS Workshop on Deep Learning and Unsupervised Feature Learning*, 2011.
- [22] Arun Pandey, Joachim Schreurs, and Johan A. K. Suykens. Robust Generative Restricted Kernel Machines using weighted conjugate feature duality. In *proceedings of the Sixth International Conference on Machine Learning, Optimization, and Data Science (LOD)*, 2020.
- [23] Arun Pandey, Joachim Schreurs, and Johan A.K. Suykens. Generative restricted kernel machines: A framework for multi-view generation and disentangled feature learning. *Neural Networks*, 135:177 – 191, 2021.
- [24] Scott Reed, Yi Zhang, Yuting Zhang, and Honglak Lee. Deep Visual Analogy-Making. In *Advances in Neural Information Processing Systems*, 2015.
- [25] Danilo Jimenez Rezende and Shakir Mohamed. Variational Inference with Normalizing Flows. *International Conference on Machine Learning (ICML)*, 2015.
- [26] M. Rolínek, D. Zietlow, and G. Martius. Variational Autoencoders pursue PCA directions (by accident). In *2019 IEEE/CVF Conference on Computer Vision and Pattern Recognition (CVPR)*, pages 12398–12407, 2019.
- [27] Ruslan Salakhutdinov and Geoffrey Hinton. Deep Boltzmann Machines. In *proceedings of the Twelfth International Conference on Artificial Intelligence and Statistics*, volume 5 of *JMLR*, 2009.
- [28] Johan A. K. Suykens. Deep Restricted Kernel Machines using conjugate feature duality. *Neural Computation*, 29(8):2123–2163, August 2017.
- [29] Han Xiao, Kashif Rasul, and Roland Vollgraf. Fashion-MNIST: A Novel Image Dataset for Benchmarking Machine Learning Algorithms. *arXiv:1708.07747*, 2017.
- [30] Yun Yang, Mert Pilanci, and Martin J. Wainwright. Randomized sketches for kernels: Fast and optimal nonparametric regression. *The Annals of Statistics*, 45(3):991–1023, 2017.